AAS 11-250

# LAGRANGIAN COHERENT STRUCTURES IN THE RESTRICTED THREE-BODY PROBLEM

**Cody R. Short[*], Kathleen C. Howell[†], and Xavier M. Tricoche[‡]**

The inherent difficulty of spacecraft mission design in regimes involving multiple gravitating bodies is somewhat alleviated by tools that provide sophisticated conceptual cues in an understandable format. Specifically, the concepts of the Finite-Time Lyapunov Exponent (FTLE) and Lagrangian Coherent Structures (LCS) are employed to visually identify regions characterized by certain behavior in a system, or to effectively isolate trajectories of potential use. The Restricted Three-Body Problem (R3BP) is a dynamical system that displays both ordered and chaotic behavior. This varied complexity is amenable to visual analysis of FTLE information and the associated LCS. Samples of FTLE/LCS visualizations highlight the applicability of these tools for mission design.

## INTRODUCTION

While brute-force methodologies can produce viable options for a given application, a more informed process often produces similar results for less effort. For spacecraft trajectories, potential solutions are frequently identified from preliminary analysis with numerical simulation. Such simulations can only yield information that is, at most, as accurate as the underlying model. The addition of factors to increase the accuracy of the model allows for more realistic solutions and a generally more representative and informative design space. However, such additional insight comes at the cost of added complexity requiring the appropriate tools for its analysis.

For astrodynamical design in some systems, an initial investigation is accomplished via numerical simulation in a model that considers the simultaneous gravitational influence of several bodies. For example, transfer design between the Earth and the Moon would likely require initial investigations based in simulations that incorporate the gravitational influence of both the Earth and the Moon. A similar situation might involve the gravitational influence of both an asteroid and a nearby planet on the motion of a spacecraft. In either case, preliminary results can be obtained by modeling in terms of a simplified three-body system. However, these initial results will likely require transition to a more realistic model. Therefore, it is convenient to employ analysis tools that can be applied to the simplified model and then be extended to the higher-order model. The concepts underlying the Finite-Time Lyapunov Exponent (FTLE) and Lagrangian Coherent Structures (LCS) can be applied to obtain information in the both the lower- and higher-fidelity models.

[*]Ph.D. Student, School of Aeronautics and Astronautics, Purdue University, 701 West Stadium Avenue, West Lafayette, IN 47907-2045.

[†]Hsu Lo Professor of Aeronautical and Astronautical Engineering, School of Aeronautics and Astronautics, Purdue University, 701 West Stadium Avenue, West Lafayette, IN 47907-2045.

[‡]Assistant Professor, Department of Computer Science, Purdue University, 305 North University Street, West Lafayette, IN 47907-2107.

The focus of this analysis is a demonstration of the applicability of the FTLE/LCS concepts and the advantages of these approaches in the Restricted Three-Body Problem (R3BP) by comparison with information obtained via alternate methods. George Haller initially introduced the concept of LCS and established its association with invariant manifolds.[1] Comparison of manifold structures and LCS in the R3BP affirms the nature of the LCS and the general predictive abilities of FTLE and similar metrics in a spacecraft mission design setting. Discussion of the visualization and computational methods employed to obtain various results serves to illustrate the balance between the fundamental conceptual simplicity and the computational expense. Further, this work serves to seed a variety of research questions and offers initial avenues for further investigation.

## THE RESTRICTED PROBLEM

Considering that many space settings of interest involve multiple gravity fields, appropriate models should include as many of these gravity fields as necessary to ensure accurate simulation. In some cases, a two-body formulation is sufficient for many important practical applications, but is less appropriate in other regimes. Moreover, a two-body formulation yields an analytical solution but may not capture some of the real-world, perceptible features of interest in a system. In contrast, models involving more than two bodies offer no analytical solutions, frequently, additional complexities exist, some of which are of a smaller effect than can be reasonably modeled. Formulating the problem in terms of three bodies produces a model sufficiently complex to reveal many important characteristics while remaining tractable. However, the general three-body problem possesses no closed-form solution.[2] Thus, additional simplifications, such as those consistent with the Circular Restricted Three-Body Problem, offer significant insight. Each of the abbreviations CR3BP, R3BP, or, simply, the restricted problem refer to the circular restricted three-body problem. The CR3BP incorporates only the effects of the masses of the two larger primaries (for example, the Earth and the Moon as they evolve on a mutual circular orbit) on a third, much smaller mass, such as a spacecraft. Despite the particular focus here on the restricted problem, the associated concepts in the investigation are not limited to such a regime.

Beyond the general description, a more careful mathematical definition for the CR3BP is important. The three bodies that appear in the model are designated as $P_1$, $P_2$, and $P_3$ – the body of interest. Position variables, $x$, $y$, and $z$ describe the position of the third body with respect to the barycenter of the primary system, which also serves as the origin of the rotating and inertial reference frames. The system mass parameter is represented by $\mu = \frac{m_2}{m_1+m_2}$, a function of the masses of the primary bodies. Additionally, distances between the third body and the two primaries are denoted $r_{i3}$. Specifically, in a coordinate frame that rotates coincident with the circular motion of the primaries, a system of differential equations that describes the motion of the third body incorporates the potential function,

$$U^* = \frac{1-\mu}{r_{13}} + \frac{\mu}{r_{23}} + \frac{1}{2}n^2(x^2+y^2), \tag{1}$$

and is written,

$$\ddot{x} = \frac{\partial U^*}{\partial x} + 2\dot{y}, \tag{2a}$$

$$\ddot{y} = \frac{\partial U^*}{\partial y} - 2\dot{x}, \tag{2b}$$

$$\ddot{z} = \frac{\partial U^*}{\partial z}, \tag{2c}$$

where the first derivatives in $x$ and $y$ appear as a result of Coriolis acceleration.

The equations of motion in the restricted problem are known to admit a single integral of the motion.[3] This integral is termed the Jacobi integral and is represented by $C$ in this analysis,

$$C = 2U^* - v^2, \tag{3}$$

where $v^2 = \dot{x}^2 + \dot{y}^2 + \dot{z}^2$, that is, the square of the magnitude of the relative velocity. This integral allows for a reduction of order in the problem, and plays an important role in the definition of FTLE maps. The Jacobi integral also implies boundaries on the motion of the third body in the restricted problem. These boundaries are defined when the velocity in Equation 3 is zero, separating regions of real and imaginary velocities. An example of these Jacobi limiting boundaries, or Zero Velocity Curves (ZVC), is depicted in Figure 1 along with the two libration points near the second primary, Saturn (50$\times$ scale), in the Sun-Saturn system.

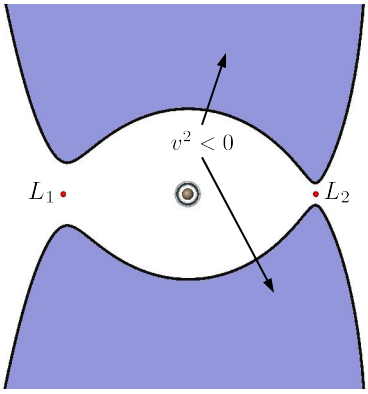


**Figure 1. Zero Velocity Curves in the $P_2$ Region**

The restricted problem represents a model of sufficient complexity to exhibit regions of both chaotic and relatively ordered behavior. Generally, the focus of the analysis is to understand and exploit behavior that is associated with the chaotic regions to identify useful trajectory arcs. The R3BP model is frequently suitable to yield first-order mission design solutions, but useful information can be difficult to isolate amidst the chaos. Investigation of Lagrangian coherent structures in the R3BP supplies additional insight for mission applications.

## LAGRANGIAN COHERENT STRUCTURES

In 2000, George Haller[1,4] as well as Haller and Yuan[5] formalized the mathematics of LCS and gave the concept its name. While there are different metrics that can be employed to identify LCS, the finite-time Lyapunov exponent is generally the most common, where relatively high values of the FTLE indicate LCS. The FTLE measures the stretching between adjacent trajectories over a prescribed time interval. Building on his own work, Haller later identified and offered additional criteria to distinguish between actual stretching and shear.[6] Shadden et al.[7] rigorously established the fundamental concept that LCS act as transport barriers in the flow by proving the flux across LCS is negligible. Mathur et al.[8] offered an effective implementation for extracting LCS, and Lekien et al.[9] established the relevance of LCS methodology in $n$-dimensional motion.

Given the well-established theoretical foundation, the popularity of LCS has quickly expanded such that active research is occurring in multiple disciplines. Simultaneous activities in computer

science and visualization seek to effectively compute and extract LCS. Specifically, work by Garth et al.,[10] featuring adaptive mesh refinement for the calculation of FTLE near structures of interest, has delivered a means to improve the time efficiency of various methods for computing LCS. Additional applications of LCS include flow structures in aeronautical weather data, transport in the oceans, computational fluid dynamics, and even human musculoskeletal biomechanics, blood circulation, and airway transport.[11]

The application of LCS in an astrodynamical context is not entirely novel. Lara et al.,[12] Villac,[13] as well as Villac and Broschart[14] all apply fast Lyapunov chaoticity indicators, a metric similar in form to FTLE, to preliminary spacecraft trajectory design and stability analysis in multi-body environments. In a more direct application, Gawlik et al.[15] offer an analysis in mixed position-velocity phase space of LCS in the planar elliptic restricted three-body problem. Each of these contributions serves to indicate the timeliness and relevance of the current analysis.

Mathematically, the calculation of the FTLE is fairly straightforward. The flow map, $\phi_{t_0}^{t}(\bar{x})$, represents the state of the system that has evolved to a final time $t$ from an initial state $\bar{x}$ at time $t_0$. This terminology and compact notation is a convenient expression for any particular solution in a system. The FTLE* is computed as the largest normalized eigenvalue of $\sqrt{\frac{d\phi_{t_0}^{t}(\bar{x})}{d\bar{x}_0}^{\mathsf{T}} \frac{d\phi_{t_0}^{t}(\bar{x})}{d\bar{x}_0}}$, i.e., the matrix spectral norm of the Jacobian ($^{\mathsf{T}}$ indicates the matrix transpose). If several adjacent, initial states are separated by small perturbations and subsequently evolved for a prescribed time, the Jacobian can be estimated as described by Shadden et al.[7] via finite differencing such as,

$$\left.\frac{d\phi_{t_0}^{t}(\bar{x})}{d\bar{x}_0}\right|_{(i,j)} = \begin{bmatrix} \frac{x_{i+1,j}(t)-x_{i-1,j}(t)}{x_{i+1,j}(t_0)-x_{i-1,j}(t_0)} & \frac{x_{i,j+1}(t)-x_{i,j-1}(t)}{y_{i,j+1}(t_0)-y_{i,j-1}(t_0)} \\ \frac{y_{i+1,j}(t)-y_{i-1,j}(t)}{x_{i+1,j}(t_0)-x_{i-1,j}(t_0)} & \frac{y_{i,j+1}(t)-y_{i,j-1}(t)}{y_{i,j+1}(t_0)-y_{i,j-1}(t_0)} \end{bmatrix}, \tag{4}$$

where the indices $i$ and $j$ indicate relative initial perturbations in $x$ and $y$, respectively. Frequently, these initial perturbations are defined with a regular grid spacing, however, such a grid spacing is not required.

With an evaluated flow map and its associated derivative, the FTLE ($\lambda$) can be calculated. Thus, the expression for the FTLE is,

$$\lambda = \frac{1}{|T|} \ln \tilde{\lambda}_{max} \left( \sqrt{\frac{d\phi_{t_0}^{t}(\bar{x})}{d\bar{x}_0}^{\mathsf{T}} \frac{d\phi_{t_0}^{t}(\bar{x})}{d\bar{x}_0}} \right), \tag{5}$$

with $\tilde{\lambda}_{max}()$ representing the operation that extracts the largest eigenvalue of the operand. The parameter $T = t - t_0$ represents both the truncation time for the FTLE and a means of normalizing the FTLE value.

In practice, an entire field of FTLE values are calculated and displayed on a map or section. In this way, comparisons of the FTLE values across a relatively large area are possible. Specifically, regions characteristic of similar FTLE values are identified while a single individual region may be markedly different, in terms of FTLE value, than other regions within the field. Bounding these regions are height ridges corresponding to relatively large FTLE values. Such ridges are defined as curves where the FTLE values are maximal with respect to the largest principle curvature. That is, ridge values

*Here *the FTLE* refers to the largest finite-time Lyapunov exponent, which, until recently,[16] has been of principle interest in FTLE/LCS analysis.

are largest with respect to the sides of the ridge but not necessarily along the top of the ridge where they may be greater or less than neighboring ridge values. Height ridges, their significance and computation, are given greater treatment by Eberly et al.[17] These FTLE ridges represent Lagrangian coherent structures, and act as boundaries in the flow separating regions of fundamentally different qualitative behavior. In autonomous systems, the LCS correspond to invariant manifolds while, in time-dependent flows, the LCS evolve with the flow while continuing to bound distinct regions of behavior.

## COMPUTATIONAL METHODS

A large part of this analysis is intended to highlight the advantages of FTLE mapping strategies. One particular way to accomplish this task is by comparison with other approaches. Investigations of trajectories or flows in the CR3BP are frequently based on explorations of the design space by propagating trajectories. One particular strategy involves constructing periapse Poincaré maps representing invariant manifolds in the restricted problem. These maps indicate the future behavior of the trajectories based upon their relative locations as observed on the map. Such a periapse Poincaré mapping of manifold structures is a focus of the work by Haapala[18] and Davis and Howell.[19] Here, comparisons with the results from Haapala are evaluated.

From various types of options, a periapse Poincaré map is constructed to identify and characterize regions of motion within the $P_2$ region. A particular advantage of the periapse map is its typical visualization in configuration space as opposed to a mixed position-velocity space. When such a map is constructed to represent manifold structures, it reveals regions where the associated flow moves in a particular way. For example, periapses that lie within a contour on the map and that are associated with the stable or unstable invariant manifolds of a periodic orbit correspond to trajectories that behave in a predictable way. Specifically, such trajectories are known to arrive in (or depart from) the $P_2$ vicinity through a region or contour that corresponds to a specific libration point. This concept of periapse contours associated with manifold structures that originate with periodic orbits is illustrated in Figure 2 (reproduced with permission from Haapala[18]). Periodic Lyapunov orbits at a specific level of Jacobi constant, $C$, are identified near libration points $L_1$ and $L_2$. Representative trajectories along the stable manifolds are plotted through their first periapsis. The manifolds themselves are designated by $W^S$, with superscript $S$ reflecting a stable manifold and $\pm$ reflecting that only "half"-manifolds are depicted. The first periapses associated with the stable manifold trajectories are indicated as blue dots near $P_2$ in the center of the figure. The periapses imply a contour that appears as a lobe. If trajectories along the unstable manifolds that are associated with the same periodic orbits are plotted in forward time, the first periapses produce different lobes. The set of *all* manifold trajectory periapses that are associated with each of the emerging contours from Figure 2(a) form individual closed lobes as is apparent in Figure 2(b). The stable manifolds yield the blue contours designated $\Gamma^S$ and numbered by subscripts; the unstable manifolds produce the red lobes labeled $\Gamma^U$. The subscripts indicate the corresponding $L_1$ or $L_2$ Lyapunov orbit as well as a number '1' identifying the fact that this contour corresponds to the first periapses along the manifold trajectories. Subsequent passes through periapses yield additional contours that are numbered successively. As a trajectory evolves in forward time, passage through the first periapse lobe guarantees a passage through the second lobe at a later time, and so on. Thus, trajectory segments suitable for a specific application are obtained by targeting a periapsis in a pre-determined region of the map. Haapala illustrates this concept by the identification of trajectories that transit the primary regions in the R3BP in a predictable pattern.[18] This identification is accomplished by the observation of the

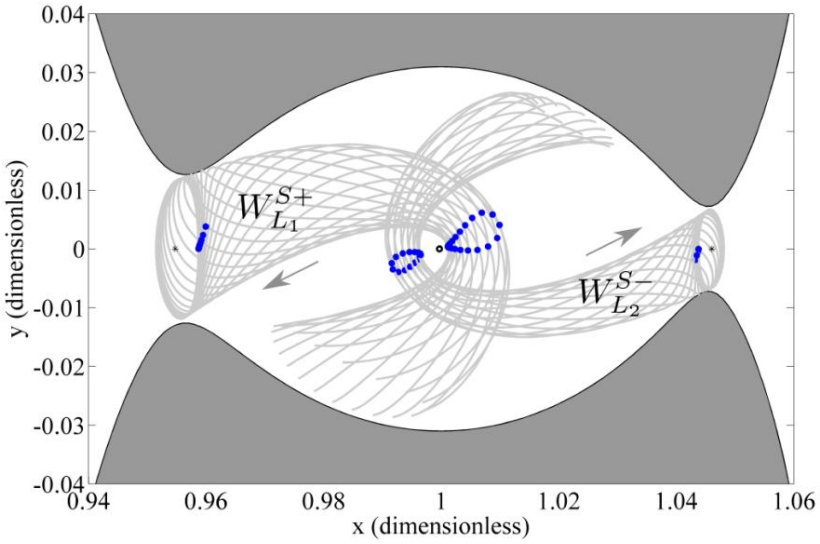


(a) A few manifold periapses

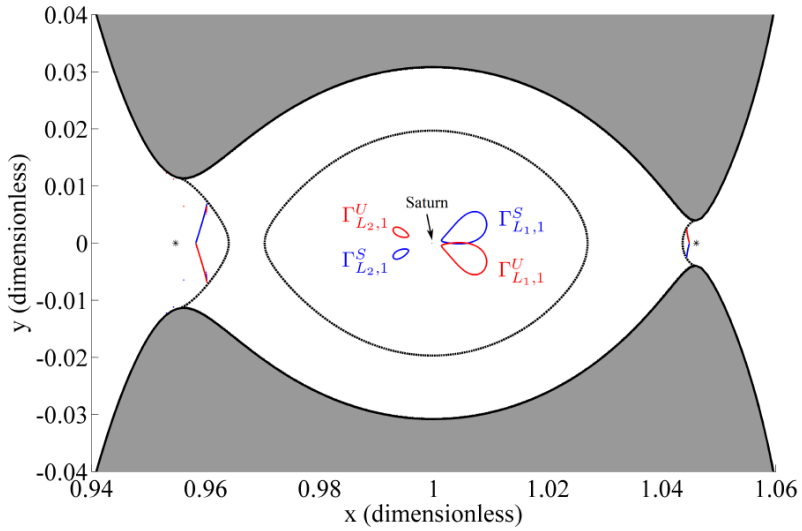


(b) Periapse lobes

**Figure 2. Emerging Manifold Periapse Lobes (with permission: A. Haapala[18])**

location of a particular periapsis with respect to the contours corresponding to stable and unstable invariant manifolds associated with periodic orbits near one of the libration points. Specifically, if a periapsis lies within a certain numbered crossing of the periapse map corresponding to the stable manifold, then it is known that the trajectory evolved into the primary region and subsequently experienced the same specified number of revolutions about the primary before arriving at the state depicted on the map. Alternatively, if the periapsis originally lies within a certain numbered cross-

ing of the unstable manifold, then the corresponding trajectory departs the current primary region after a specified number of revolutions about the primary. Finally, if a periapsis lies in a set of lobes or contours that intersect, i.e., contours that are associated with both a stable manifold and an unstable manifold, then the past evolution into the region as well as the future evolution out of the region is established.

A zoomed region of a manifold periapse Poincaré map from Haapala[18] characteristic of a specific Jacobi constant value, $C = 3.01740$ in the Sun-Saturn ($\mu \approx 2.85804 \times 10^{-4}$) R3BP appears as Figure 3. In Figure 3, stable manifold periapse crossings of the map are indicated as blue dots while unstable manifold crossings of the map enclose a specific region and are colored in red. Recall, the manifold structures or contours are labeled with the symbol $\Gamma$ with superscripts $U$ and $S$ indicating unstable and stable manifolds, respectively. The red contour in Figure 3 is indeed the $\Gamma^U_{L_1,1}$ contour from Figure 2(b). The subscript, $L_1$, identifies these manifold structures as those associated with a periodic orbit in the vicinity of the $L_1$ libration point. The stable manifold associated with the $L_1$ Lyapunov orbit is propagated in reverse time. The contours corresponding to the first periapses ($\Gamma^S_{L_1,1}$) intersect the "top" of the red lobe, while subsequent contours, $\Gamma^S_{L_1,i}$, intersect the red lobe in successively "lower" regions. These intersections between the manifolds are colored by their respective crossings, where different solid-colored regions indicate subsequent intersections of the stable manifold and the unstable manifold contours as indicated by subscript indices (1-6).

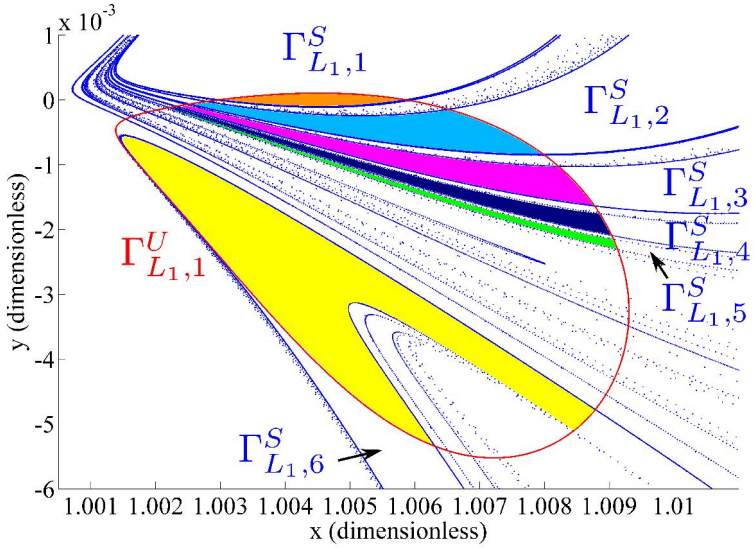


**Figure 3. Periapse Poincaré Map of Manifold Periapse Crossings (with permission: A. Haapala[18])**

This type of periapse Poincaré map supplies information regarding boundaries on the motion because the stable and unstable invariant manifolds act as separatrices in the flow for the planar restricted problem.[18,20] To produce such a map, knowledge of the invariant manifolds is required. Subsequent calculation and display of the manifolds on the map reveals various behaviors in different locations, but generally supplies little information regarding the variation of behavior within the region or contour. Information regarding the variation of behavior interior to these regions of interest is generated by seeding the Poincaré map differently, that is, by adding seed points other than those associated with the manifolds. Unfortunately, it is difficult to seed the map such that a simulation predictably returns to a desired area of the map. Therefore, alternate methods are employed to complement this mapping approach.

Maps of FTLE values are generally defined by selecting a region and discretizing the region into a set of grid points. The states associated with the grid points serve as the seed points for evaluating the flow map. Subsequent calculation of FTLE values from the flow map supplies a field of values for the selected region. Comparison of these values indicates regions of qualitatively different motion bounded by Lagrangian coherent structures. The flow map evolves throughout an interval that depends on the associated application, however, a longer interval allows greater detail to emerge in the FTLE map. For the present comparison, maps are terminated after a specified number of successive periapse crossings as well as a uniform time. A periapse FTLE map corresponding to the manifold map from Figure 3 appears as Figure 4.

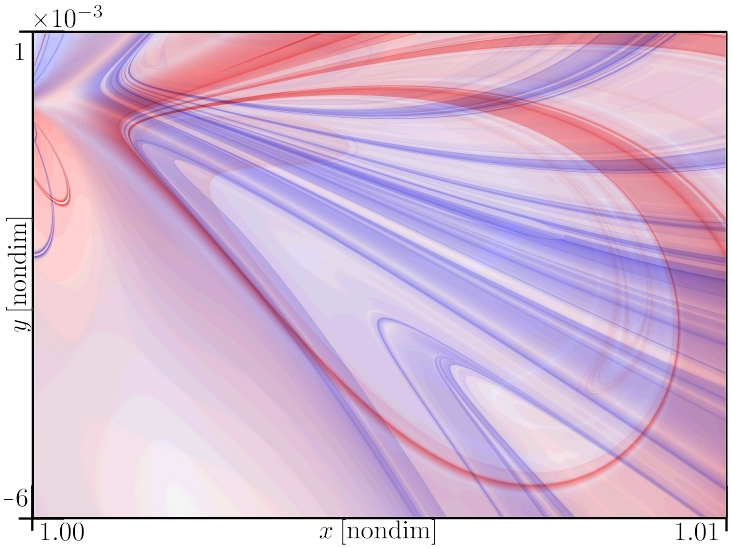


**Figure 4. Periapse FTLE Associated with the Manifold Map from Figure 3**

In Figure 4, forward-time FTLE are colored by their relative values in blue and backward-time FTLE are colored in the same manner in red. The brightest colors in Figure 4 correspond to the highest associated FTLE values, while an FTLE value of zero is represented in white. Finally, locations of both high forward FTLE and high backward FTLE values are colored black. This color mapping is illustrated in Figure 5 and is used throughout the document. These colors are selected to reflect the correspondence of forward FTLE structures with the stable manifolds and backward FTLE structures with the unstable manifolds in Figure 3.

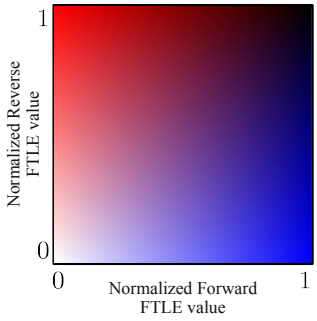


**Figure 5. Color Map Employed for FTLE Maps**

This particular FTLE figure (Figure 4) illustrates one approach to calculate such a FTLE map. Specifically, the flow map is required to terminate after a certain number of periapse passages, where periapse passages are defined consistent with Haapala[18] as well as Davis and Howell[19] such that, if the position and velocity of the spacecraft relative to $P_2$ are defined as,

$$\bar{q} = \begin{bmatrix} x - 1 + \mu & y & z \end{bmatrix}^{\mathsf{T}}, \tag{6}$$

$$\dot{\bar{q}} = \begin{bmatrix} \dot{x} & \dot{y} & \dot{z} \end{bmatrix}^{\mathsf{T}}, \tag{7}$$

then the conditions for periapses are,

$$\bar{q}\dot{\bar{q}}^{\mathsf{T}} = (x + 1 - \mu)\dot{x} + y\dot{y} + z\dot{z} = 0, \tag{8}$$

$$v^2 + \bar{q}\ddot{\bar{q}}^{\mathsf{T}} = (\dot{x}^2 + \dot{y}^2 + \dot{z}^2) + (x - 1 + \mu)\ddot{x} + y\ddot{y} + z\ddot{z} \geq 0. \tag{9}$$

In the present case, the forward FTLE (blue) is generated after six crossings of the periapse map while the reverse FTLE (red) results from termination of the flow map after three periapse passages. In general, it is desirable to run such an FTLE simulation for longer times because more structure is apparent with additional integration time. However, in this analysis, the objective is the evaluation of the information in a periapse FTLE map that is terminated after stopping conditions that are similar to the manifold map. Direct comparison of the periapse Poincaré maps (manifold and FTLE) as well as a comparison between the manifold periapse map with FTLE over a constant time are evaluated.

For the calculation of a constant time FTLE map, the flow map is evaluated for a consistent time across the field. This allows more direct comparison between neighboring trajectories where the periapse FTLE map reveals specific information about changes in the evolution of the periapse structures between neighboring trajectories. Both cases reveal useful information.

For consistency, the evaluation of the flow map for calculation of all FTLE results in this paper is completed using a single integration scheme, a Runge-Kutta-Fehlberg (RKF) $4^{\text{th}}/5^{\text{th}}$ order integrator with adaptive step size error control. Moreover, the prescribed integration tolerances are set to maintain integration error to the order of $10^{-12}$. The specific RKF implementation employed is from the GNU Scientific Library.[21]

Given the highly parallel nature of evaluating the flow map on a grid, two types of parallelization are employed to help mitigate the associated computational cost. Namely, parallelization on the Graphics Processing Unit with NVIDIA® Compute Unified Device Architecture (CUDA™)[22] to obtain lower accuracy preliminary results followed by parallelization on a multi-core CPU platform with OpenMP[23] to produce higher accuracy, double precision maps.

The resulting values for forward and backward FTLE produce a two-dimensional field of scalar values. This type of scalar field is amenable to visualization. Throughout this analysis, FTLE maps are visualized with Teem,[24] a specialized data manipulation and visualization package. Trajectories associated with the maps are displayed in Avizo®, a visualization package from Visualization Sciences Group (VSG).[25] Intermediate visualization and image exploration are performed with interactive graphical tools developed specifically for this investigation. Ultimately, visualization allows for an immediate picture of the flow from which trajectories with certain behaviors are isolated.

## ANALYSIS

Comparison of FTLE maps generated in the course of this investigation with existing maps highlights some of the advantages of FTLE approaches. Comparison between periapse Poincaré manifold and FTLE maps is detailed. Then, a comparison of FTLE maps for various time durations is summarized.

Recall the yellow region from Figure 3. This region is also apparent in Figure 4. All of the points within the red lobe are first crossings of trajectories that enter the $P_2$ region through the $L_1$ gateway; this conclusion results from the fact that all such points lie within the red boundary, i.e., the first unstable crossing of the manifold associated with the $L_1$ Lyapunov orbit. Overlaid on the red lobe are backward crossings of the map by the stable manifold emanating from the same orbit. Recall that the colored ribbons identify a particular crossing number where yellow implies the $6^{\text{th}}$ periapse crossing. Within the area of the FTLE map (Figure 4) that corresponds to the yellow band from Figure 3, note the region of relatively larger FTLE values running diagonally along the edge of the lobe. The information associated with the FTLE map in this region is not captured in the associated Poincaré manifold plot. Other structures also appear that originate with flow in this region that are not previously captured in the periapse maps. Two zoomed views focus on specific areas of this region and appear as insets in Figure 6. These specific areas are identified due to the presence of intersecting FTLE. The intersections are represented by green dots in Figure 6 and the corresponding states are listed in Table 1. These states are evolved forward and backward in time until they effectively meet, and the associated trajectories, along with zoomed views of the Saturn region in the Sun-Saturn system, appear in Figures 7 and 8. Note that both the Sun and Saturn appear scaled $100\times$ and $20\times$, respectively, in these figures. Corrections are required to join the arcs at the point of discontinuity given the manual point identification from the associated image. Thus, these intersections, readily identified from the FTLE data and not immediately apparent from an associated manifold Poincaré plot, immediately produce compelling results in the form of orbits that pass back and forth between the two primary regions in the Sun-Saturn system.

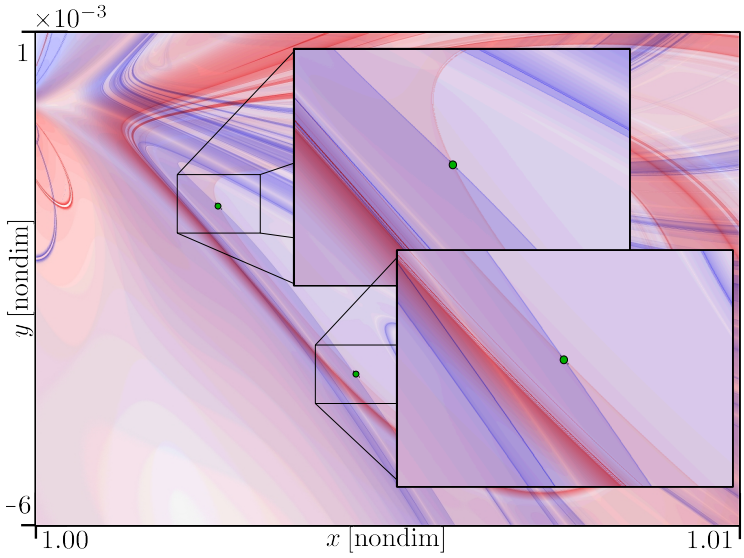


**Figure 6. Zoomed Insets Focused on Regions of Interest from Figure 4**

**Table 1. Point Data Selected Manually from Figure 6 for Inspection**

| Inset | $[x\ y\ z\ \dot{x}\ \dot{y}\ \dot{z}]^\mathsf{T}$ (non-dim) | $[x\ y\ z\ \dot{y}\ \dot{y}\ \dot{z}]^\mathsf{T}$ (km $\times 10^9$ \| km/s) | Figure No. |
|---|---|---|---|
| Top | $[1.002602\ -0.001474\ 0.0\cdots$ $0.180594\ 0.353733\ 0.0]^\mathsf{T}$ | $[1.430439\ -0.002104\ 0.0\cdots$ $1.742012\ 3.412110\ 0.0]^\mathsf{T}$ | 7 |
| Bottom | $[1.004517\ -0.003834\ 0.0\cdots$ $0.170356\ 0.213345\ 0.0]^\mathsf{T}$ | $[1.433169\ -0.005471\ 0.0\cdots$ $1.643254\ 2.057928\ 0.0]^\mathsf{T}$ | 8 |

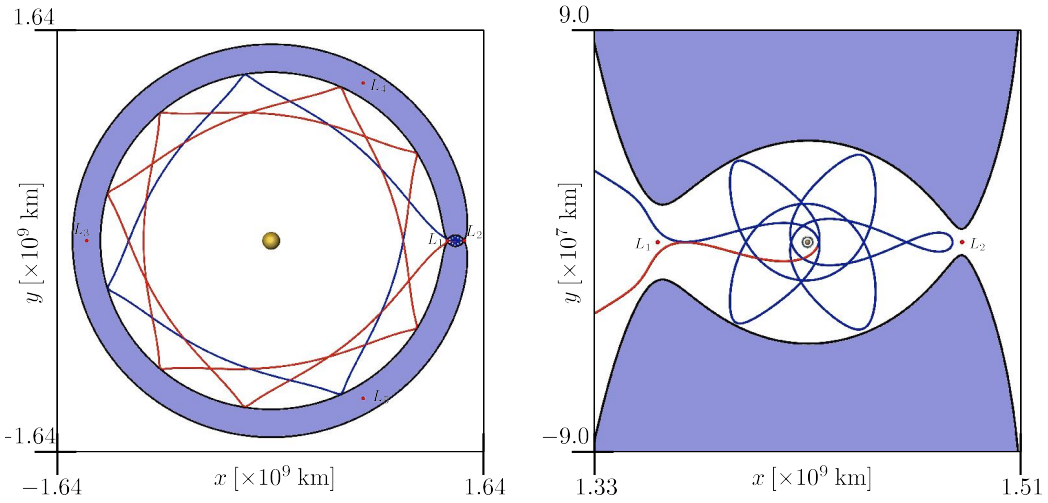


(a) Wide view showing both the primary regions (b) Zoom focused on Saturn region from (a)

**Figure 7. Trajectories from Green Point in Top Inset of Figure 6**

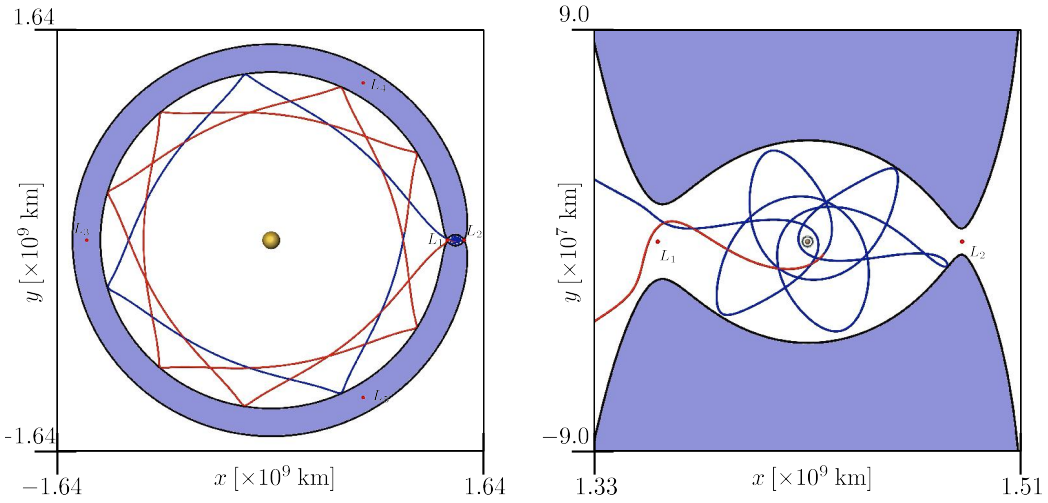


(a) Wide view showing both the primary regions (b) Zoom focused on Saturn region from (a)

**Figure 8. Trajectories from Green Point in Bottom Inset of Figure 6**

In addition to these trajectories, several trajectories selected along both sides of a structure in the region discussed above highlight different behavior on opposite sides of the structure. In Figure 9, which corresponds to the top inset from Figure 6, trajectories below the structure are indicated by red dots, while trajectories above the contour are depicted in blue. Each of the trajectories below the contour exhibit behavior consistent with that depicted in Figure 10(a), while those above the contour all display an evolution like that shown in Figure 10(b). Both trajectories in Figure 10 were terminated after six periapses with respect to the smaller primary (Saturn). However, in the Figure 10(a) the trajectory's inflection is such that periapse conditions as described by Equation 8 occur on the far side of the Sun while in Figure 10(b) this is not the case. This comparison illustrates the power of the FTLE and indicates the nature of an LCS boundary. The different qualitative behavior observed by two trajectories from relatively nearby initial states, but on opposite sides of a LCS are seen to exhibit different behavior under the parameters of the simulation.

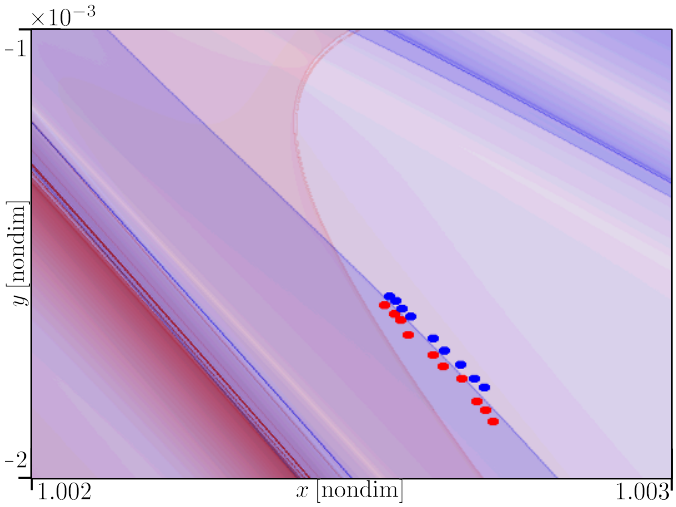


**Figure 9. Points That Represent Trajectories Above and Below a Map Contour**

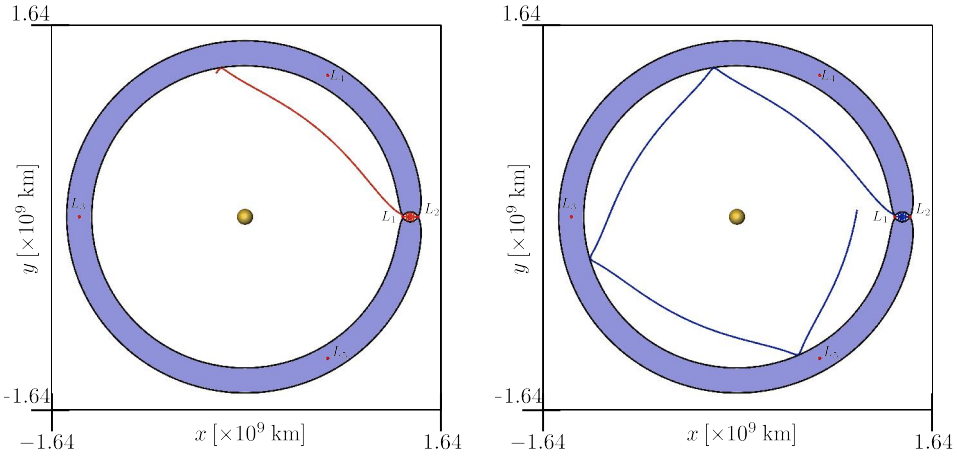


(a) A red-point trajectory from Figure 9

(b) A blue-point trajectory from Figure 9

**Figure 10. Trajectories on Opposite Sides of a Forward LCS Contour (blue) in Figure 9**

Another region from Figure 4 reveals structure not apparent in the manifold maps. Specifically, faint 'loops' of red (backward-time) FTLE are apparent along the right side of the unstable lobe. This additional structure also appears in a constant time duration FTLE map given sufficient simulation time. Further investigation of these structures is pending.

The comparison of the manifold and FTLE periapse maps indicates how the dense output associated with FTLE maps can supply immediate additional insight toward the behavior for any position on the map. However, a more common application of FTLE maps employs what is effectively a single iteration of a stroboscopic map, that is, the flow map evaluated at the same final time for all initial states. This type of map supplies information pertaining to the stretching of nearby trajectories at a specified later time. An example of such a map in the same region of the Sun-Saturn system associated with the previous results appears as Figure 11. The FTLE values in Figure 11 and the

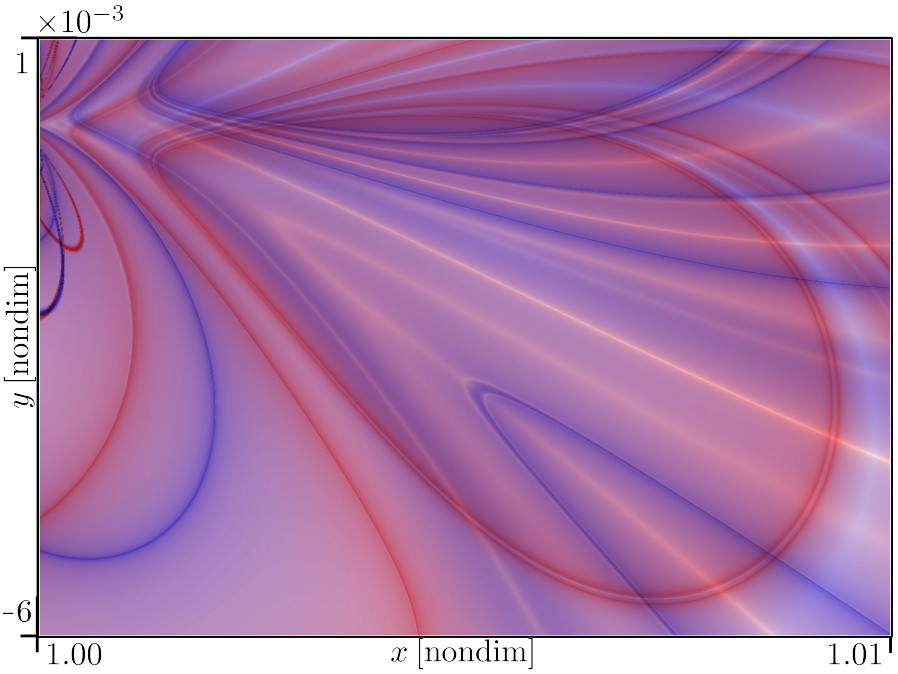


**Figure 11. Fixed-Time FTLE Map for a Duration of ∼23.43 years (5 ND time steps)**

subsequent figures are calculated consistent with Equations 4 and 5, that is, via finite differencing to approximate the Jacobian in $x$ and $y$. It is apparent that the structure associated with the six crossings of the periapse map has yet to develop, however other types of structure are seen throughout the image. Longer duration maps appear in Figure 12 and 13 corresponding to time intervals of ∼46.89 years (10 ND time steps) and ∼234.35 years (50 ND time steps), respectively. From these later maps, no structure corresponding to the strip along the edge of the unstable manifold inspected previously is apparent. The 'looping' structures alluded to previously are apparent in Figure 13. One of the most useful types of information readily available on these maps is stability information indicated by white regions. It is apparent from the previous figures that such relatively stable regions exist even over longer durations, such as in Figure 13. Ultimately, these regions of stability as well as the other regions indicated by LCS in the FTLE represent the power of these types of maps to supply general insight for the overall flow in a system of interest.

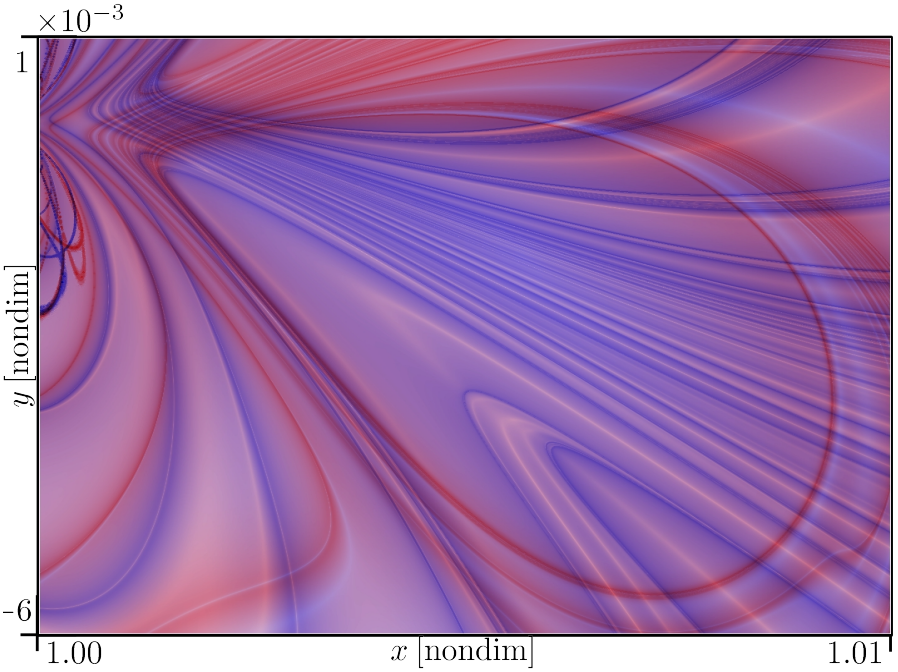


**Figure 12. Fixed-Time FTLE Map for a Duration of ∼46.89 years (10 ND time steps)**

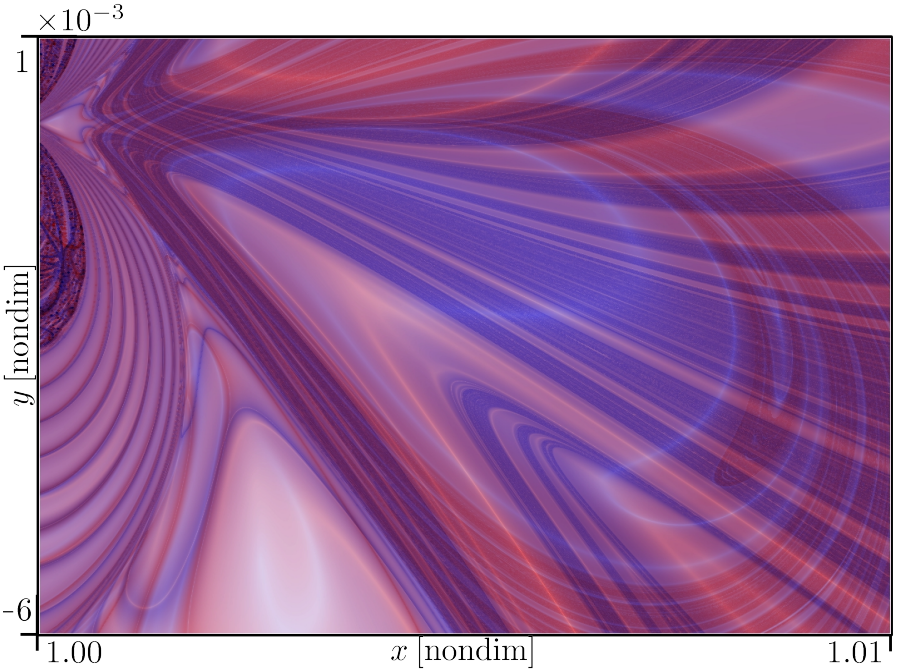


**Figure 13. Fixed-Time FTLE Map for a Duration of ∼234.35 years (50 ND time steps)**

## CONCLUSION

The various examples shown in this work illustrate the usefulness of FTLE/LCS analysis as a tool for mission design. While this initial study deals only with systems described by a simplified three-body model, the restricted three-body problem, the associated concepts extend directly into more complicated models of multi-body motion. In some ways, this paper represents an initial investigation to develop the methodology to extend the concepts of FTLE and LCS to other models. In the present analysis it is readily apparent that a simple tool such as the FTLE provides direct information regarding the behavior of neighboring trajectories, and when this information is visually accessible, such as if displayed on a map, an overall picture of the flow results. From this visualization, motion boundaries are discernible without requiring previous knowledge of their existence. Finally, the picture provided by FTLE maps immediately provides new "blanket" insight useful for making mission design decisions.

## ACKNOWLEDGMENTS

This work was conducted at Purdue University. Partial support was provided by assistantships from the Schools of Aeronautics and Astronautics and Engineering Education as well as the Rune and Barbara Eliasen Aerospace Visualization Laboratory.

## REFERENCES

[1] G. Haller, "Finding finite-time invariant manifolds in two-dimensional velocity fields," *Chaos*, Vol. 10, No. 1, 2000, pp. 99–108.

[2] F. Diacu, "The Solution of the *n*-body Problem," *The Mathematical Intelligencer*, Vol. 18, No. 3, 1996, pp. 66–70.

[3] V. Szebehely, *Theory of Orbits: The Restricted Problem of Three Bodies*. New York: Academic Press, 1967.

[4] G. Haller, "Distinguished material surfaces and coherent structures in three-dimensional fluid flows," *Physica D*, Vol. 149, 2001, pp. 248–277.

[5] G. Haller and G. Yuan, "Lagrangian coherent structures and mixing in two-dimensional turbulence," *Physica D*, Vol. 147, 2000, pp. 352–370.

[6] G. Haller, "Lagrangian coherent structures from approximate velocity data," *Physics of Fluids*, Vol. 14, No. 6, 2002, pp. 1851–1861.

[7] S. C. Shadden, F. Lekien, and J. E. Marsden, "Definition and properties of Lagrangian coherent structures from finite-time Lyapunov exponents in two-dimensional aperiodic flows," *Physica D*, Vol. 212, 2005, pp. 271–304.

[8] M. Mathur, G. Haller, T. Peacock, J. Ruppert-Felsot, and H. Swinney, "Uncovering the Lagrangian Skeleton of Turbulence," *Physical Review Letters*, Vol. 98, 2007, pp. 144502–1–4.

[9] F. Lekien, S. C. Shadden, and J. E. Marsden, "Lagrangian coherent structures in n-dimensional systems," *Journal of Mathematical Physics*, Vol. 48, 2007, pp. 065404–1–19.

[10] C. Garth, F. Gerhardt, X. Tricoche, and H. Hagen, "Efficient Computation and Visualization of Coherent Structures in Fluid Flow Applications," *IEEE Transactions on Visualization and Computer Graphics*, Vol. 13(6), 2007, pp. 1464–1471.

[11] T. Peacock and J. Dabin, "Introduction to focus issue: Lagrangian coherent structures," *Chaos*, Vol. 20, 2010, pp. 017501–1–3.

[12] M. Lara, R. P. Russell, and B. Villac, "Classification of the Distant Stability Regions at Europa," *Journal of Guidance, Control, and Dynamics*, Vol. 30, No. 2, 2007, pp. 409–418.

[13] B. F. Villac, "Using FLI maps for preliminary spacecraft trajectory design in multi-body environments," *Celestial Mechanics and Dynamical Astronomy*, Vol. 102, No. 1-3, 2008, pp. 29–48.

[14] B. Villac and S. Broschart, "Applications of Chaoticitiy Indicators to Stability Analysis Around Small Bodies," *$19^{th}$ AAS/AIAA Space Flight Mechanics Meeting*, Savannah, Georgia, February 9-12, 2009. Paper No. AAS 09-221.

[15] E. S. Gawlik, J. E. Marsden, P. C. du Toit, and S. Campagnola, "Lagrangian coherent structures in the planar elliptic restricted three-body problem," *Celestial Mechanics and Dynamical Astronomy*, Vol. 103, No. 3, 2009, pp. 227–249.

[16] G. Haller and T. Sapsis, "Lagrangian coherent structures and the smallest finite-time Lyapunov exponent," 2010. preprint, available at `http://georgehaller.com/reprints/smallestFTLE.pdf`.

[17] D. Eberly, R. Gardner, B. Morse, and S. Pizer, "Ridges for Image Analysis," *Journal of Mathematical Imaging and Vision*, Vol. 4, 1994, pp. 355–371.

[18] A. F. Haapala, "Trajectory Design Using Periapse Maps and Invariant Manifolds," M.S. Thesis, School of Aeronautics and Astronautics, Purdue University, West Lafayette, Indiana, 2010.

[19] D. C. Davis and K. C. Howell, "Trajectory Evolution in the Multi-Body Problem with Applications in the Saturnian System," *IAF 61st International Astronautical Congress*, Prague, Czech Republic, September, 2010. Paper No. IAC-10-C1.1.7.

[20] S. Wiggins, L. Wiesenfeld, C. Jaffé, and T. Uzer, "Impenetrable Barriers in the Phase-Space," *Physical Review Letters*, Vol. 86, 2001, pp. 5478–5481.

[21] "The GNU Scientific Library Manual," [Online Publication, retrieved 24 Aug 2010], `http://www.gnu.org/software/gsl/manual/html_node/index.html`, 2010.

[22] "NVIDIA® CUDA™ Architecture, Version 1.1," [Online Publication, retrieved 8 Nov 2010], `http://developer.download.nvidia.com/compute/cuda/docs/CUDA_Architecture_Overview.pdf`, April, 2009.

[23] "The OpenMP API Specification for Parallel Programming," [Online Publication, retrieved 4 Oct 2010], `http://openmp.org/wp/about-openmp/`, 2010.

[24] "Teem: Tools to process and visualize scientific data and images," [Online Publication, retrieved 12 Oct 2010], `http://teem.sourceforge.net/`, 2010.

[25] "Avizo®—VSG," [Online Publication, retrieved 24 Jan 2011], `http://www.vsg3d.com/avizo/overview`, 2010.